Inelastic Scattering of Electrons by Protons*

A. A. Cone,† K. W. Chen,‡ J. R. Dunning, Jr.,§ G. Hartwig,** Norman F. Ramsey,
J. K. Walker, and Richard Wilson
Harvard University, Cambridge, Massachusetts

(Received 7 December 1966)

The inelastic scattering of electrons by protons has been measured at incident electron energies up to 5 BeV/c and momentum transfers $q^2=4(\text{BeV}/c)^2$. Excitation of known nucleon resonances at $M=1238$, 1512, 1688, and possibly 1920 MeV have been observed. The calculations for the resonance at $M=1238$ MeV have been compared with calculations by Adler based on the dispersion theory of Chew, Goldberger, Low, and Nambu. The agreement is good. Qualitative models are discussed for the other resonances.

INTRODUCTION

THE inelastic scattering of electrons was shown by Franck and Hertz to be a useful technique for studying atomic structure. By studying the energy spectrum of scattered electrons, they were able to measure the excitation spectrum of atoms. In the terminology of modern high-energy physics, this would now be called missing mass spectroscopy.

The application of this method to the study of the proton and its excited states was begun by Panofsky and Allton[1] and was extended by Hand.[2] These authors studied the excitation of the pion-nucleon (nucleon excited state) at a mass of 1240 MeV and with quantum numbers, $I=\frac{3}{2}$, $J=\frac{3}{2}^+$ up to a momentum transfer $q^2=18$ F^{-2} $[0.7(\text{BeV}/c)^2]$. Hand failed to find evidence of excitation of other resonances.

In this work, the excitation of the 1240-MeV resonance is studied up to a momentum transfer $q^2=90$ F^{-2} $[3.61(\text{BeV}/c)^2]$ and the excitation of the resonances at masses of 1512, 1690, and 1920 MeV are observed. These are compared with such theoretical calculations as are available. There is good agreement except for the excitation of the resonance at 1512 MeV, which is too great to be understood. This paper extends and supersedes a preliminary communication of these results.[3]

KINEMATICS AND ONE-PHOTON EXCHANGE

Throughout this paper we will use a notation close to that of Hand.[2] Some of the kinematic quantities are clear from the diagram of Fig. 1. At these momentum transfers, elastic scattering is believed to proceed primarily by one-photon exchange. It is therefore reasonable to assume that the inelastic scattering also proceeds by one-photon exchange. Then the cross section for inelastic scattering can be shown to be separable[2]:

$$d^2\sigma/d\Omega dE_f=\Gamma_{\text{transverse}}(\theta,q^2,K)\sigma_{\text{transverse}}(q^2,K)+\Gamma_{\text{scalar}}(\theta,q^2,K)\sigma_{\text{scalar}}(q^2,K), \quad (1)$$

where

$$\Gamma_{\text{transverse}}=\Gamma_T=\frac{\alpha}{4\pi^2}\frac{K}{q^2}\frac{E_f}{E_i}\left[2+\frac{\cot^2(\theta/2)}{1+(q_0^2/q^2)}\right],$$

$$\Gamma_{\text{scalar}}=\Gamma_0=\frac{\alpha}{4\pi^2}\frac{K}{q^2}\frac{E_f}{E_i}\frac{\cot^2(\theta/2)}{[1+(q_0^2/q^2)]},$$

$$K=q_0-q^2/2M=(M^{*2}-M^2)/2M.$$

We abbreviate $\sigma_T\equiv\sigma_{\text{transverse}}$; $\sigma_0\equiv\sigma_{\text{scalar}}$.

The relation between K and M^* is independent of the 4-momentum transfer q^2. At $q^2=0$ (photoproduction), K is the laboratory photon energy. For electroproduction, it is therefore called the virtual photon energy.

In the metric used here, the square of the 4-momentum transfer is positive for scattering:

$$q^2=4E_iE_f\sin^2(\tfrac{1}{2}\theta). \quad (2)$$

If we use quantities in the center-of-mass system of the outgoing nucleon system M^*, we find the fourth component of the 4-vector q:

$$q_0^*=(M^{*2}-M^2)/2M^*-q^2/2M^*, \quad (3)$$

whereas, in the laboratory,

$$q_0=(M^{*2}-M^2)/2M+q^2/2M. \quad (4)$$

The normalization of the Γ factors is such that

$$\sigma_T(0,K)=\sigma_\gamma(K), \quad (5)$$

which is the photoproduction cross section at the

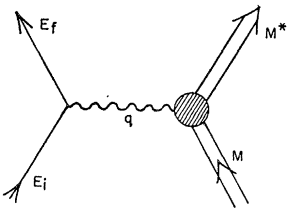

FIG. 1. A diagram to aid in understanding the kinematics of inelastic ep scattering.

* Supported by the U. S. Atomic Energy Commission.
† Present address: Vancouver City College, Vancouver, B. C.
‡ Present address: Palmer Physical Laboratory, Princeton University, Princeton, New Jersey.
§ Supported by the National Science Foundation.
** Present address: Deutsches Elektronen-Synchrotron, Hamburg, Hamburg, Germany.

[1] W. K. H. Panofsky and E. Allton, Phys. Rev. **110**, 1155 (1958).
[2] L. N. Hand, Phys. Rev. **129**, 1834 (1963).
[3] A. A. Cone, K. W. Chen, J. R. Dunning Jr., G. Hartwig, N. F. Ramsey, J. K. Walker, and Richard Wilson, Phys. Rev. Letters **14**, 326 (1965).

photon energy K. The Γ factors have the dimensions of the number of virtual photons per BeV steradian.

The experimental aim is therefore to determine $\sigma_T(q^2,K)$ and $\sigma_0(q^2,K)$ over a range of values of q^2 and K (or, equivalently, q^2 and M^*).

APPARATUS

The experiment was done concurrently with the experiments on elastic electron-proton and quasielastic electron-deuteron scattering previously reported,[4] and used the same apparatus.

The electrons from the internal beam of the Cambridge electron accelerator impinged on a liquid-hydrogen target; the scattered electrons passed through a quadrupole spectrometer onto a scintillation counter bank. A threshold Čerenkov counter and a shower counter helped to distinguish electrons from pions. Pions could only be detected by knock on (π-e scattering) in the Čerenkov counter and by charge exchange in the shower counter.

Figures 2 and 3 are, respectively, vertical and horizontal schemes of the experimental setup. The liquid-hydrogen target was contained in a vertical cylinder of Mylar or Dupont H film which was centered about $\frac{3}{4}$ in. inside the equilibrium orbit of the circulating beam. At the end of the acceleration cycle, the rf was turned off and the electrons spiraled inward until they penetrated the target. The incident flux was monitored by a quantameter and an ion chamber which observed the forward bremsstrahlung from the electron beam hitting the target.

The scattered electrons passed through a single quadrupole magnet with a center plug and were focused along a horizontal line. Several long, thin scintillation counters were arranged parallel to this line, thus making available several momentum acceptance bins simultaneously. Placed after these "slat" counters, as they were called, was a gas Čerenkov counter which was used as a threshold counter to distinguish electrons from heavier charged particles. Finally, there were two large scintillation counters, the latter of which was used as a shower counter to distinguish the high-energy scattered electrons from low-energy knock-on electrons and pions.

An electron was counted when the following conditions were met. Counters C_1, C_8, and either C_{8a}, C_{7a} or

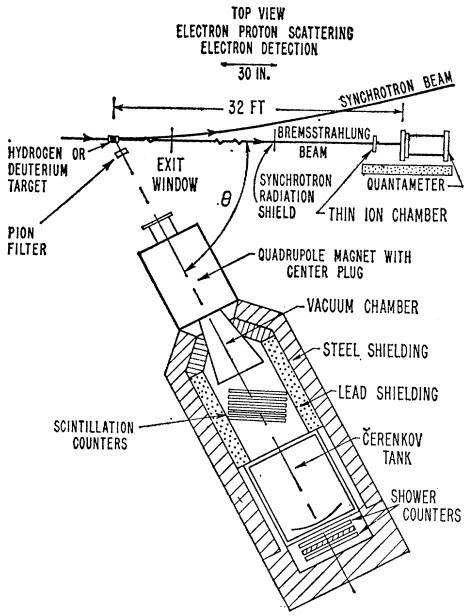

FIG. 2. Layout of the experimental apparatus, top view.

C_{8b}, C_{7B} had to register in coincidence, which meant a charged particle had crossed the median plane of the quadrupole magnet somewhere between C_8 and C_7. Such an event was called a fourfold count. A count from C_9 was demanded in coincidence with this; such an event was called a fivefold count. A count from the Čerenkov counter in coincidence with a fivefold opened a gate to the pulse-height analyzer to receive the output from the shower counter C_{10}. If the signal from the shower counter was above the bias level set for it, then the coincidence of fivefold plus Čerenkov plus C_{10}, called a slat drive signal, was produced. If a slat counter, i.e., counters C_2 through C_6, registered in coincidence with the slat drive signal, an electron count was registered in the appropriate momentum bin.

This apparatus has been described in great detail in Ref. 4. Some additional details of importance for the inelastic spectrum follow.

Spectrometer Calibration

The magnetic-field gradient and effective length of the quadrupole magnet as a function of current were

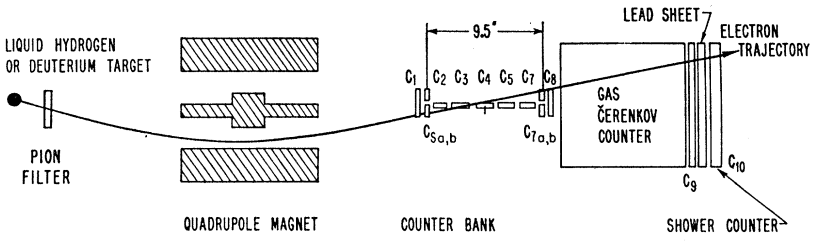

FIG. 3. Arrangement of counters showing a typical electron trajectory, side view.

[4] K. W. Chen, J. R. Dunning, A. A. Cone, N. F. Ramsey, J. K. Walker, and Richard Wilson, Phys. Rev. 141, 1267, 1286 (1966).

supplied to an accuracy of 0.2% by Paul Cooper, Jr. These were measured by a long flip coil and by Hall-probe measurements. A graphical interpolation of these points was the basis for calculating the curve of scattered energy focused at a distance of 63 in. from the face of the magnet (the center of C_4 in Fig. 3) versus the current through the magnet. This curve was recalibrated by noting the position of the elastic peak as a function of the spectrometer current. The recalibrated curve shows that the magnet did not saturate as rapidly as the interpolation of Cooper's data would suggest.

At the focal point of 63 in., the average percentage change in momentum is 0.718% per inch.

Now the slat counters (C_2 through C_6 in Fig. 3) were 1.5-in. wide in the direction of momentum resolution, and this corresponds to about 1.1% for dp/p. However, because of their finite height ($\frac{1}{16}$ in.), the slats detected particles outside this momentum bite. Therefore, in order to compute the momentum resolution properly, the efficiency of the slat counters must be taken into account. The method is as follows. Take a portion of the spectrum which is relatively flat. Let N equal the number of bins in which counts are accepted. Suppose there are really n counts per bin. Then Nn is the ideal total number of counts. Let f be the fractional overlap on one side of a slat into the next bin. Let S equal the sum of the actual slat counts; let T equal the total in peak, i.e., the number of events which triggered any or all of the slats simultaneously. Then we have

$$Nn(1+2f)=S,$$

and

$$Nn+n2f=T; \tag{6}$$

hence

$$2f=N(S-T)/(NT-S).$$

Then 1.08% times $(1+2f)$ is the actual dp/p for the slats.

This method implies no more than about a 5% error in the momentum bite per slat.

The Counter Bank Tilt

The small but finite angular acceptance of the spectrometer led to a spread in the energy of scattered electrons. During the experiment, the slats were tilted in the horizontal plane so that all the elastic events would appear in one slat (neglecting resolution function and radiative tails for the present). The same tilt of the counter bank also ensured that all inelastically scattered electrons of the same value of K appeared in the same slat. We see this from a kinematic calculation as follows:

$$E'=\frac{E-K}{1+(E/M)(1-\cos\theta)},$$

$$\frac{\partial E'}{\partial\theta}=-E'\frac{(E/M)\sin\theta}{1+(E/M)(1-\cos\theta)},$$

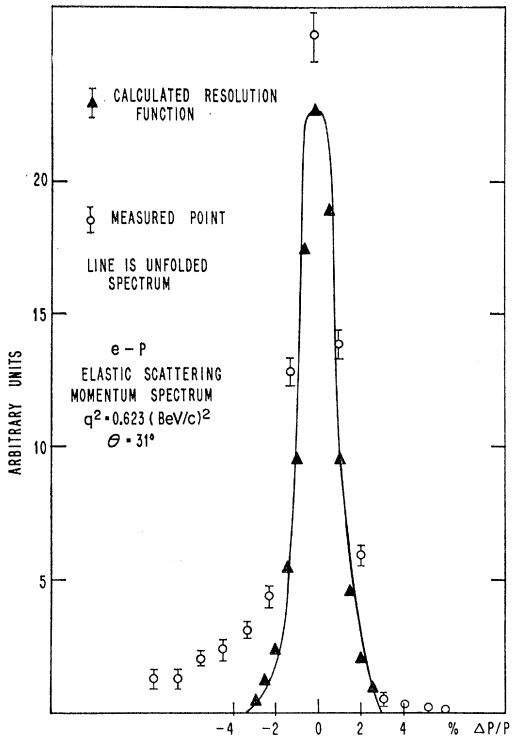

FIG. 4. Comparison of the calculated and measured resolution function of the spectrometer.

therefore,

$$\frac{\partial E'}{E'}=-\frac{(E/M)\sin\theta}{1+(E/M)(1-\cos\theta)}d\theta, \tag{7}$$

which is independent of E' and K for constant E.

Figure 4 shows the calculated resolution of the spectrometer compared with the measured elastic scattering.

Pion Rejection

High-energy pions have a mean free path of about 8 in. in lead and could, therefore, be counted in the spectrometer not only by traversing the spectrometer according to the design, but also by penetrating the shielding and the central plug. The background of these pions was very large.

Pions could count in the threshold Čerenkov counter by their knock-on electrons, particularly if they had penetrated the absorber. They could count in the shower counter by charge exchange. It was important to ensure that pions were not being detected in this experiment.

In the elastic-scattering experiment,[3] absolute cross sections were measured. Accordingly, it was necessary to detect small pulses in the Čerenkov counter and shower counter to ensure their efficiency. Only relative measurements were needed in this work, so that only events with large pulses in both the shower counter and Čerenkov counter were included.

A lead filter of $\frac{1}{2}$-in. Pb (3 radiation lengths) was inserted in the scattered beam near the target at each momentum setting of the spectrometer. With this thickness, no more than 1% of the electrons emerge with energies greater than one-half of the incident energy; since we only studied electrons from half the elastic scattered energy upwards, this filter effectively removes the electrons. However, high-energy pions are reduced by only 10%.

It was verified that this filter indeed leaves the pions by observing the background without the Čerenkov counter, or shower counter, or at a momentum setting above the elastic peak where only pions penetrating the shielding or scattering off the pole tips could count. The background was hardly affected by the presence of the filter. We were, therefore, able to show that the background of pions was always less than 10% of the total counts and usually close to zero. When we tried to observe excitation of the mass 1512-MeV resonance at $\theta=90°$ and $q^2=1$ (BeV/c)^2, the background as determined by the lead filter was too large and the attempt was abandoned.

Radiative Corrections

This has been called, in the past, the correction for wide-angle bremsstrahlung. We prefer to regard it as part of a general radiative correction calculation.

Although the most thorough discussion of radiative processes is that of Bjorken,[5] an easier procedure to follow is described by Perez y Jorba.[6] Experimentally, we measure a cross section $\sigma_{\text{meas}}(E_i,E_f)=d^2\sigma/(d\Omega dE_f)$ for finding a scattered electron of energy E_f. We are interested in a hypothetical cross section which we would measure if there were no radiative processes. Electrons radiate both before and after scattering. Thus, $\sigma_{\text{meas}}(E_i,E_f)$ includes contributions from $\sigma(E_i,E_f')$ (where $E_f'>E_f$) weighted by a radiation kernel $K_A(E_f',E_f)$ for radiation of a photon of energy $E_f'-E_f$ (radiation after scattering). Similarly, there is a term in $\sigma(E_i',E_f)$ for $(E_i>E_i')$ which is due to radiation *before* scattering. There is also the usual Schwinger correction which corresponds to inelastic events $\sigma(E_i,E_f)$ with radiation out of the detector bin width Δ.

According to the Perez y Jorba recipe, therefore,

$$\sigma_{\text{meas}}(E_i,E_f)=\sigma(E_i,E_f)(1-\delta)+\int_0^{E_i-\Delta E}K_B(E_i,E_i')\sigma(E_i',E_f)dE_i'+\int_{E_f+\Delta E}^{\infty}K_A(E_f',E_f)\sigma(E_i,E_f')dE_f', \quad (8)$$

where $\sigma(E_i,E_f)$ is the cross section for scattering without radiating, $(1-\delta)$ is the Schwinger correction term, K_B is the radiation kernel for radiation before scattering, and K_A is that for radiation after scattering. These K's are calculated in the peaking approximation using the formula developed by Hand.[2]

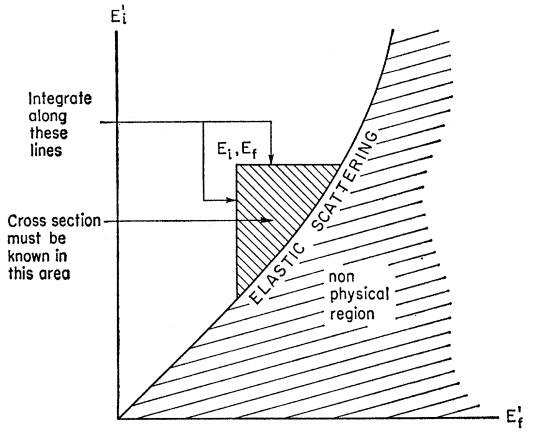

FIG. 5. A kinematic diagram relating the incident and final electron energies, showing the region that must be measured to make a radiative correction.

Here δ is given by

$$\frac{2\alpha}{\pi}\left[\left(\ln\frac{E_f}{\Delta E}-\frac{13}{12}\right)\left(\ln\frac{q^2}{m^2}-1\right)+\frac{17}{36}\right],$$

$$K_A=\frac{E_i'}{E_i}\frac{\alpha}{\pi}\frac{1}{E_i-E_i'}\left\{\ln\frac{q^2}{m^2}-1+\frac{(E_i-E_i')^2}{E_i^*-E_i'}\times\left[\ln\frac{2E_i}{m}-\tfrac{1}{2}\ln\left(1+\frac{2E_i}{M}\right)\right]\right\}, \quad (9)$$

$$K_B=\frac{E_f}{E_f'}\frac{\alpha}{\pi}\frac{1}{E_f'-E_f}\left\{\ln\frac{q^2}{m^2}-1+\frac{(E_f'-E_f)^2}{E_f'E_f}\times\left[\ln\frac{2E_f}{m}-\tfrac{1}{2}\ln\left(1+\frac{2E_f}{M}\right)\right]\right\}.$$

Here Δ is the bin width at the detector.

We must also add a small (5%) addition to K_A, K_B, and δ for the real physical radiators present in the experiment.

Thus to evaluate the corrected cross section $\sigma(E_i,E_f)$, we must know $\sigma(E_i,E_f')$ at all values of E_f' from E_f up to the elastic scattering value and $\sigma(E_i',E_f)$ at all values of E_i' from E_i down to the elastic-scattering value. The correction thus becomes an iterative procedure.

This is made clear by reference to Fig. 5. This is a kinematic diagram of the incident energy versus the scattered energy. Clearly, all elastic-scattering events lie on a line on this plot. Inelastic events all lie to the left of this line, with smaller E_f.

[5] J. S. Bjorken, Ann. Phys. (N. Y.) 24, 201 (1963).
[6] J. Perez y Jorba, Orsay Report No. 1108, 1964 (unpublished).

When we consider the determination of the correction for a point, E_i, E_f in this plot, we see that the line integrals of Eq. (8) are the horizontal and vertical lines in this figure. Now, since we need to know $\sigma(E_i,E_f)$ at every point on the line, we see we must know $\sigma_{\text{meas}}(E_i,E_f)$ at all points in the shaded region before we may start the iteration.

$\sigma(E_i,E_f)$ is clearly known for elastic scattering by using the form factors from Ref. 3; for inelastic scattering, it may be determined at any momentum transfer and K using data for lower momentum transfers and lower K. For the evaluation we must interpolate between known points. This is done using Eq. (1) for the inelastic or elastic scattering and interpolating the elastic form factors according to Ref. 2 and the inelastic cross section σ_T according to the formula $G_M\nu^2(q)^{2l}$, where the value of l is chosen from the two known points at the end of the interpolation range. This procedure approximates the expected theoretical behavior of the cross section.

The radiative corrections have been evaluated using different bin sizes Δ and using slightly different radiation kernals K_A, K_B. The results are insignificantly different.

Attempts were made to calculate the radiative correction according to the recipe of Bjorken.[5] However, the results gave $\sigma\simeq 1.1\ \sigma_{\text{meas}}$, contrary to physical intuition and to the Perez y Jorba calculation, which gives $\sigma\simeq 0.9\ \sigma_{\text{meas}}$. The two methods should be equivalent (see the Appendix), though that of Bjorken is harder to apply. We believe that our attempts to calculate with the Bjorken recipe were subject to an unknown source of error and should, therefore, be ignored.

TREATMENT OF DATA

Two principal subtractions are to be made on the raw data, viz., target-wall scattering and the radiative corrections. Subtraction of detected pions in the scattered beam was carried out by the lead-filter technique described above and was always small. Electrons arising from charge-symmetric processes (e.g., Dalitz pairs) were subtracted off by observing the positron cross section at various points along the spectra. This subtraction was also small. The subtracted counts had to be corrected for the shower-counter efficiency at the particular bias and energy of the electron. These efficiencies were measured by observing the shower-counter spectrum for elastically scattered electrons at comparable energies.

False kinematic coincidences such as that diagrammed in Fig. 6 were suppressed by demanding a signal from one of the slat counters. The recipe followed then was: (1) to obtain the counts from hydrogen alone after wall subtraction; (2) to subtract counts with the field reversed; (3) to correct for background pions using the lead filter; (4) to normalize the inelastic counting rates to an absolute cross section by comparing them with the elastic counting rate; (5) to correct for shower counter efficiency; and (6) to compute the radiative corrections.

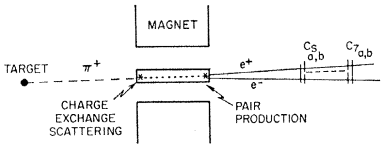

FIG. 6. Illustration of a process that could produce a false count if care is not taken.

Target-Wall Backgrouud

The fractions of electrons scattered from the target wall varied from 10 to 20% of the total scattering. This fraction was determined by measuring the distribution of the beam across the target using the beam clipper as described in Ref. 3; from this we deduce directly the fraction of bremsstrahlung from the hydrogen, G. The calculation then proceeds as follows.

Let N be the number of counts for a given run, Q the charge collected by the quantameter, and $R=N/Q$ the counts per unit charge. More precisely, let N_H^- equal the number of positron counts in the reversed field subtraction, N_H^+ equal the number of positron counts in the reversed field runs. Let $N_M^\pm$ be similarly defined for the Mylar cup of the H film (target-wall scattering). Let Q_H equal the quantameter charge due to bremsstrahlung in the hydrogen, let Q_M be the same for the target wall. Let $G=Q_H/(Q_H+Q_M)$ be the fraction of bremsstrahlung for H_2.

This G is obtained from a knowledge of the shape of the target cup and measurements of the amount of bremsstrahlung as a function of the amount of target exposed to the beam.

Note then that the raw counting rate R_0 is given by

$$R_0=\frac{N_H^-+N_H^++N_M^-+N_M^+}{Q_H+Q_M}. \tag{10}$$

The counting rate from the solid target of the same material as the target wall is also measured;

$$R_M=(N_M^-+N_M^+)/Q_M. \tag{11}$$

This should be the same number for the target wall alone. The reversed field for H_2 plus target wall is

$$R_0^+=(N_H^++N_M^+)/(Q_H+Q_M). \tag{12}$$

The reversed field for the target wall alone is

$$R_M^+=N_M^+/Q_M. \tag{13}$$

The number that is wanted is

$$R_H^-=N_H^-/Q_H. \tag{14}$$

Solving for this in terms of the measured quantities, we obtain

$$R_H^-=G^{-1}[(R_0-R_0^+)-(1-G)(R_M-R_M^+)]. \tag{15}$$

Consider the two limiting cases:

$$(A)\quad R_M^+=0,$$
$$R_H^-=G^{-1}[R_0-(1-G)R_M]-R_0^+/G, \qquad (16)$$

$$(B)\quad R_M^+=R_H^+,$$
$$R_H^-=G^{-1}[R_0-(1-G)R_M]-R_0^+. \qquad (17)$$

In practice, there is not much difference, since R_0^+ is always about 5% or less of R_0.

The correction is listed as a multiplicative correction and includes the correction to the monitoring as well as that due to scatter from the walls. This somewhat disguises its real form, which we therefore now discuss. From Eq. (17), we note that when $G=0.9$ (90% of the bremsstrahlung from hydrogen which is true for $E=5$ BeV) and $R_M=R_0$, we have 10% of the scatters due to the target walls, yet the multiplicative correction is near unity. The correction differs from unity when the fraction of events scattered from the target walls is different from the fraction of the bremsstrahlung from the walls.

TABLE I. Differential cross sections for $E_i=2.358$ BeV.

E_f[a] (BeV)	R[b]	ST[c]	RAD[d]	σ (10^{-32} cm²/BeV sr)	Δ[e] (%)
1.774	0.213	1.27			
1.754	0.598	1.40			
1.735	0.862	1.43			
1.716	0.485	1.38			
1.698	0.160	1.17			
1.680	0.119	1.04			
1.662	0.084	0.83			
1.643	0.0758	0.745	0.350	0.260	10
1.624	0.0955	0.881	0.398	0.446	14
1.607	0.0800	0.744	0.652	0.523	14
1.591	0.109	0.928	0.833	1.155	12
1.573	0.116	0.948	0.938	1.435	12
1.556	0.145	1.046	1.027	2.187	11
1.539	0.189	1.142	1.072	3.295	10
1.522	0.236	1.204	1.045	4.267	8
1.506	0.293	1.254	1.078	5.813	7
1.490	0.277	1.234	1.072	5.436	7
1.473	0.352	1.284	1.018	6.904	6
1.457	0.274	1.222	0.937	4.756	6
1.441	0.230	1.171	0.993	4.104	6
1.426	0.233	0.977	0.920	3.286	7
1.411	0.203	1.200	0.894	3.440	7
1.395	0.213	1.106	0.880	3.322	7
1.380	0.208	1.026	0.881	3.049	7
1.365	0.194	1.122	0.879	3.126	8
1.350	0.196	1.187	0.885	3.454	8
1.336	0.207	1.032	0.900	3.255	7
1.321	0.194	1.344	0.891	3.970	7
1.307	0.225	0.991	0.906	3.501	7
1.292	0.201	1.252	0.915	4.023	7
1.279	0.219	1.078	0.928	3.919	7
1.265	0.209	1.196	0.921	4.165	7
1.250	0.219	1.351	0.936	5.054	7
1.237	0.249	1.141	0.950	4.982	6
1.223	0.241	1.412	0.945	6.019	5
1.210	0.279	1.125	0.953	5.720	5
1.197	0.262	1.188	0.947	5.717	4
1.184	0.259	1.275	0.953	6.221	4
1.117	0.273	1.142	0.932	5.830	4
1.158	0.260	1.079	0.892	5.110	4
1.146	0.239	1.133	0.911	5.120	4
1.134	0.232	1.157	0.874	4.954	4
1.121	0.231	1.064	0.888	4.686	4
1.109	0.215	1.150	0.862	4.669	5
1.097	0.216	1.103	0.861	4.564	5
1.085	0.209	1.164	0.858	4.753	5
1.074	0.212	1.114	0.873	4.797	5
1.106	0.207	1.446	0.863	6.154	5
1.050	0.254	1.080	0.889	5.464	4
1.039	0.239	1.238	0.889	6.022	4
1.027	0.255	1.092	0.896	5.851	4
1.016	0.245	1.110	0.842	5.490	4
1.005	0.242	1.267	0.874	6.576	4
0.994	0.283	1.076	0.862	5.690	4
0.983	0.283	1.005	0.837	5.237	4
0.973	0.270	1.150	0.867	6.002	4
0.962	0.288	1.052	0.874	5.976	4
0.952	0.283	1.033	0.857	5.730	4
0.942	0.275	1.037	0.862	5.720	4
0.931	0.271	0.828	0.847	4.478	5
0.922	0.231	1.019	0.852	4.790	4
0.912	0.239	1.090	0.833	5.251	5
0.901	0.255	0.947	0.841	5.002	6
0.891	0.243	0.954	0.818	4.733	7
0.882	0.236	1.126	0.826	5.555	7
0.872	0.259	0.959	0.802	5.121	7
0.863	0.248	1.116	0.809	5.831	7
0.853	0.268	0.673	0.789	3.757	7
0.844	0.203	1.026	0.794	4.421	7
0.835	0.221	0.919	0.776	4.285	7
0.826	0.219	0.760	0.781	3.575	7
0.817	0.194	0.971	0.764	4.017	7
0.808	0.209	0.838	0.769	3.816	7
0.799	0.200	0.982	0.752	4.252	8
0.790	0.215	0.969	0.757	4.615	8
0.782	0.223	0.753	0.761	3.801	7
0.774	0.196	1.092	0.743	4.480	7
0.765	0.227	0.699	0.749	3.650	7
0.757	0.190	0.831	0.732	3.610	7
0.748	0.190	0.657	0.736	2.918	8
0.740	0.167	0.762	0.716	2.953	8
0.732	0.169	1.114	0.722	4.482	8
0.724	0.211	0.728	0.727	3.729	8
0.716	0.186	0.882	0.707	3.948	8
0.709	0.193	0.886	0.711	4.198	8
0.701	0.196	0.782	0.716	3.864	8
0.693	0.184	1.076	0.697	4.941	8
0.686	0.212	0.738	0.701	3.996	8
0.679	0.183	0.756	0.681	3.480	8
0.671	0.169	0.763	0.686	3.335	8
0.664	0.161	1.055	0.691	4.496	8
0.657	0.187	0.857	0.669	4.173	8
0.649	0.178	0.598	0.674	2.853	8
0.642	0.140	0.826	0.679	3.178	9
0.635	0.145	0.988	0.657	3.855	9
0.628	0.161	0.858	0.662	3.822	9
0.622	0.157	0.911	0.666	4.039	9
0.615	0.158	0.808	0.640	3.528	9
0.608	0.146	0.766	0.646	3.179	9
0.602	0.133	0.804	0.652	3.131	9
0.595	0.129	1.200	0.616	4.339	9
0.589	0.159	0.765	0.624	3.522	9
0.582	0.135	0.641	0.633	2.596	9
0.576	0.110	1.222	0.587	3.825	10
0.570	0.140	0.895	0.596	3.701	10
0.563	0.133	0.691	0.605	2.805	10
0.557	0.108	1.269	0.555	3.938	10

[a] Scattered energy.
[b] Electron events per quantameter count.
[c] Correction factor for target-cup scattering.
[d] Radiative correct factor.
[e] Statistical error.

Absolute Normalization

The data were taken in such a way that absolute cross sections were obtained. In this paper we do not discuss the details of solid-angle determination, monitoring, etc., which are fully treated in Ref. 3. For convenience, the data consisting of a set of values of R were normalized to the elastic cross sections measured in Ref. 2 by the formula

$$\frac{d^2\sigma}{d_A dE_f}=\left(\frac{d\sigma}{d_A}\right)_{\text{elastic (Ref. 4)}}\frac{R_{\text{inel}}}{R_{\text{el}}}\frac{1}{\Delta E_f}, \qquad (18)$$

where ΔE_f is the bin width.

DATA

The data are presented in Tables I, II, and III at incident energies (E_i) of 2.358, 2.988, and 4.874 BeV, respectively. The laboratory scattering angle (θ) is 31° in each case.

Column 1 contains the values of the scattered energy at which electrons were detected. This scattered energy, E_f is the central energy of the detection bin. The actual bin widths were 0.0157, 0.0146, and 0.0144 times E_f for Tables I, II, and III, respectively. For each table, the third entry for E_f is the elastic scattered energy.

Column 2 contains the observed counting rate, electron events per quantameter count, for electrons scattered from the hydrogen-filled Mylar cup.

TABLE II. Differential cross sections for E_i=2.988 BeV.

E_f (BeV)	R	ST	RAD	σ (10^{-32} cm²/BeV sr)	Δ (Error in %)
2.098	0.202	1.135			
2.076	0.630	1.252			
2.054	0.877	1.268			
2.032	0.644	1.249			
2.010	0.334	1.169			
1.988	0.191	1.044			
1.966	0.154	0.960			
1.945	0.131	0.876			
1.924	0.101	0.706			
1.904	0.074	0.953	0.468	0.255	13
1.883	0.216	1.006	0.860	0.622	7
1.863	0.286	1.075	0.991	1.025	6
1.843	0.381	1.128	1.062	1.55	5
1.823	0.464	1.156	1.083	1.99	4
1.803	0.465	1.151	1.072	1.99	3
1.783	0.405	1.121	1.027	1.65	4
1.764	0.401	1.114	0.972	1.55	4
1.745	0.390	1.103	0.930	1.44	4
1.726	0.339	1.063	0.909	1.19	4
1.707	0.373	1.080	0.905	1.34	4
1.688	0.372	1.074	0.904	1.35	4
1.670	0.388	1.078	0.916	1.45	4
1.652	0.393	1.076	0.928	1.49	4
1.634	0.413	1.083	0.937	1.62	4
1.617	0.428	1.087	0.943	1.71	4
1.599	0.428	1.083	0.956	1.78	4
1.581	0.508	1.115	0.944	2.14	4
1.564	0.541	1.124	0.960	2.36	4
1.547	0.576	1.133	0.980	2.62	4
1.531	0.656	1.152	0.984	3.08	3
1.515	0.650	1.148	0.951	2.98	3
1.498	0.567	1.120	0.907	2.45	3
1.481	0.588	1.126	0.940	2.68	3
1.465	0.548	1.108	0.897	2.37	3
1.449	0.522	1.097	0.878	2.21	3
1.433	0.561	1.108	0.872	2.42	3
1.418	0.559	1.105	0.882	2.46	3
1.403	0.548	1.110	0.872	2.40	3
1.388	0.561	1.110	0.889	2.53	3
1.372	0.629	1.123	0.901	2.97	3
1.357	0.639	1.124	0.905	3.08	3
1.342	0.667	1.129	0.904	3.27	3
1.328	0.625	1.116	0.903	3.05	3
1.314	0.684	1.130	0.892	3.38	3
1.300	0.682	1.129	0.875	3.34	3
1.286	0.647	1.116	0.884	3.22	3
1.272	0.679	1.124	0.859	3.34	3
1.258	0.611	1.102	0.832	2.88	3
1.244	0.601	1.096	0.845	2.89	3
1.231	0.609	1.098	0.820	2.88	3
1.217	0.579	1.085	0.809	2.72	3.5
1.204	0.577	1.082	0.811	2.75	3.5
1.191	0.556	1.072	0.804	2.64	3.5
1.178	0.574	1.077	0.794	2.73	4.0
1.165	0.575	1.075	0.799	2.78	4.0
1.152	0.568	1.069	0.786	2.72	4.8
1.140	0.563	1.065	0.774	2.68	5.5
1.128	0.562	1.061	0.778	2.71	5.5
1.115	0.528	1.043	0.764	2.49	5.5
1.103	0.600	1.074	0.772	2.99	6
1.091	0.557	1.054	0.755	2.68	6
1.079	0.577	1.063	0.733	2.75	6
1.068	0.557	1.051	0.743	2.69	5.2
1.056	0.557	1.050	0.721	2.65	5.2
1.045	0.532	1.036	0.729	2.56	5.2
1.033	0.496	1.013	0.707	2.39	5.5
1.022	0.556	1.046	0.717	2.72	5.5
1.011	0.545	1.039	0.690	2.59	5.5
1.000	0.533	1.030	0.659	2.45	5.5
0.989	0.488	1.002	0.671	2.25	6
0.978	0.503	1.025	0.647	2.30	6
0.967	0.483	0.995	0.654	2.20	6
0.957	0.487	0.995	0.645	2.21	6
0.947	0.500	0.998	0.645	2.31	6
0.937	0.500	0.993	0.637	2.30	5
0.927	0.450	0.952	0.642	2.03	6
0.917	0.460	0.956	0.621	2.04	6
0.907	0.487	0.973	0.630	2.27	6
0.897	0.433	0.927	0.603	1.85	6
0.887	0.533	0.998	0.612	2.55	6
0.877	0.472	0.956	0.576	2.06	6
0.867	0.517	0.985	0.590	2.42	6
0.858	0.472	0.951	0.538	1.97	6
0.849	0.437	0.919	0.555	1.85	6
0.840	0.487	0.958	0.502	1.98	6
0.831	0.430	0.908	0.517	1.73	6
0.822	0.425	0.901	0.531	1.78	6
0.813	0.393	0.864	0.476	1.44	6
0.804	0.403	0.872	0.494	1.57	6
0.795	0.438	0.938	0.436	1.65	6
0.786	0.393	0.855	0.451	1.42	6
0.778	0.443	0.905	0.400	1.55	6
0.770	0.380	0.837	0.412	1.23	6
0.761	0.373	0.825	0.426	1.29	6
0.753	0.377	0.826	0.379	1.19	6

Column 3 contains the correction factor to be applied because of target-cup scattering. It is computed, using Eq. (15), and is equal to R_H^-/R_0.

Column 4 contains the correction factor to be applied because of radiative corrections. This is computed using the Perez y Jorba recipe and is equal to $\sigma/\sigma_{\text{meas}}$. In practice, the data for σ_{meas} were graphically smoothed, and thus interpolated for equally spaced values of E_f, viz., $\Delta E_f = 0.020$ BeV. This value of ΔE_f was about the same size as that of the bin width, and was small enough to show the structure of the resonances. Then for each of these values of E_f, the correction factor $\sigma/\sigma_{\text{meas}}$ was obtained and this factor was then interpolated (linearly) to the actual value of E_f that appears in column 1.

Column 5 contains the final value of the nonradiative inelastic cross section $d^2\sigma/d\Omega dE_f$ and is expressed in 10^{-32} cm^2/BeV sr.

Column 6 contains the statistical error in percent. These are listed separately from the systematic errors, so that the shape of the spectrum can be easily seen.

The following systematic errors also appear. These, however, will not produce spurious peaks.

For the radiative corrections, we expect the error to vary from 5% for the 1238 resonance to about 15% for the most inelastic regions. The error comes from the peaking approximation used, and we have estimated pessimistically the uncertainty at the higher resonances since the correction depends on previously corrected data and also on interpolated corrected data.

An error of 5% is assigned to the type of energy bin width determination as discussed near Eq. (16a), viz., the overlapping of the slat counters.

The uncertainty resulting from the hysteresis of the magnet is less than 0.1%.

The remaining contribution to the systematic error is the uncertainty in the measured elastic-cross-section sections used to normalize the inelastic data. These were given as 8%, 8.5%, and 14% for $E_i = 2.358$, 2.988, and 4.874 BeV, yielding for the total systematic errors 11 to 18%, 11 to 18%, and 16 to 22%.

Normalizing factors [cf. Eq. (18)] were found to be conveniently expressed as

$$F = d\sigma/d\Omega|_{\text{obs}} \times 1/R_{\text{el}} w E_f ,$$

where $wE_f = \Delta E_f$. The values of F are $21.4/E_f$, $6.21/E_f$, and $57.9/E_f$, respectively.

An additional error of at most 0.3% was introduced into the bin width by averaging over the five slats after a given energy bin was centered on each in turn, because the tilt of the slat counters to the perpendicular to the magnet axis was neglected and because the dispersion in energy was approximated by a constant, viz., $\Delta E_f/E_f = 0.00718$ per inch.

This value of $\Delta E_f/E_f$ per inch was the average for the dispersion through a distance of 6 in. centered about the central slat and was the same for effective lengths of the magnet of 54, 53, and 52 in.

TABLE III. Differential cross section[a] for $E_i = 4.874$ BeV.

E_f (BeV)	R	ST	RAD	σ (10^{-32} cm^2/BeV sr)	Δ (Error %)
2.858	0.00104	1.035			
2.828	0.00154	1.062			
2.798	0.00226	1.081			
2.768	0.00162	1.060			
2.738	0.00063	0.949			
2.708	0.00056	0.884			
2.678	0.00058	0.972	0.977	0.0118	38
2.649	0.00103	1.206	1.045	0.0285	26
2.620	0.00182	0.900	1.158	0.0418	17
2.592	0.00243	1.013	1.131	0.0622	12
2.564	0.00233	0.995	1.098	0.0574	11
2.536	0.00192	0.956	0.961	0.0402	12
2.509	0.00198	0.951	0.967	0.0419	12
2.482	0.00211	0.944	0.981	0.0457	11
2.455	0.00262	0.971	1.040	0.0623	10
2.428	0.00266	0.964	1.059	0.0649	10
2.401	0.00418	1.018	1.083	0.1112	8
2.375	0.00397	1.005	1.063	0.1034	8
2.349	0.00438	1.010	1.050	0.1143	8
2.324	0.00450	1.007	1.040	0.1174	8
2.299	0.00482	1.009	1.015	0.1243	7
2.274	0.00503	1.008	1.009	0.1305	7
2.249	0.00490	1.000	1.001	0.1264	7
2.224	0.00506	0.998	0.997	0.1312	7
2.201	0.00614	1.016	1.013	0.1660	7
2.177	0.00631	1.015	0.997	0.1700	6
2.153	0.00564	0.998	0.988	0.1496	6
2.130	0.00643	1.008	0.979	0.1726	5
2.107	0.00654	1.006	0.970	0.1755	5
2.084	0.00608	0.993	0.958	0.1607	5
2.061	0.00594	0.986	0.936	0.1540	4
2.038	0.00644	0.993	0.963	0.1750	4
2.016	0.00692	1.000	0.961	0.1911	4
1.994	0.00710	1.002	0.956	0.1974	4
1.973	0.00736	1.006	0.946	0.2054	4
1.951	0.00706	1.000	0.935	0.1960	4
1.930	0.00730	1.004	0.933	0.2055	4
1.909	0.00769	1.010	0.933	0.2197	4
1.888	0.00753	1.007	0.921	0.2142	4
1.868	0.00745	1.007	0.904	0.2102	4
1.848	0.00686	0.995	0.889	0.1906	4
1.828	0.00710	0.998	0.883	0.1985	4
1.808	0.00768	1.007	0.884	0.2190	4
1.179	0.00778	1.008	0.882	0.2242	
1.769	0.00758	1.006	0.879	0.2194	4
1.750	0.00727	1.002	0.877	0.2114	4
1.731	0.00807	1.014	0.875	0.2398	4
1.712	0.00791	1.014	0.872	0.2365	4
1.693	0.00804	1.016	0.865	0.2416	4
1.676	0.00778	1.012	0.860	0.2342	4
1.657	0.00804	1.016	0.851	0.2429	4
1.640	0.00838	1.019	0.833	0.2514	4
1.622	0.00814	1.017	0.848	0.2508	5
1.604	0.00743	1.007	0.829	0.2241	5
1.586	0.00694	0.998	0.804	0.2036	7
1.569	0.00787	1.014	0.776	0.2286	7

[a] These data are normalized to an elastic scattering cross section 0.8 of Ref. 4 because of new measurements of elastic scattering.

That the effect of this error on the resolution function is negligible can easily be seen by superimposing five resolution functions, each similar to Fig. 4 and displaced one after the other by 0.15%.

Figures 7, 8, and 9 show the differential cross sections as functions of scattered energy for incident energies of 2.358, 2.988, and 4.874 BeV, respectively, and scattering angles of 31° before radiative corrections have been made, i.e., only the target-wall corrections have been

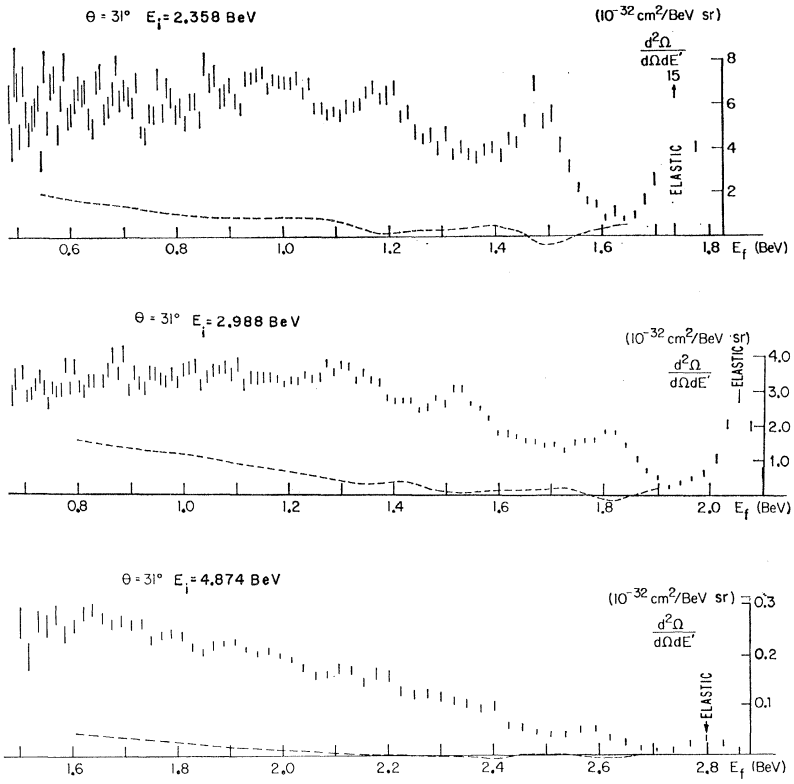

FIG. 7. Spectrum of inelastically scattered electrons for $\theta=31°$ and $E_i=2.358$ BeV (data of Table I). The dashed line shows the radiative correction applied.

FIG. 8. For Fig. 7, $\theta=31°$, $E_i=2.988$ BeV (data of Table II).

FIG. 9. For Fig. 7, $\theta=31°$, $E_i=4.874$ BeV (data of Table III). These data are normalized to an elastic scattering cross section 0.8 of Ref. 4 because of new measurements of elastic scattering.

applied. The radiative correction, in the form $(\sigma_{\text{meas}}-\sigma)$ is represented by the dashed line.

The G factor, as used in Eq. (16) for the target-wall scattering correction, had the values 0.670, 0.760, and 0.890 for the three incident energies, respectively.

Other data, shown in Table IV, including the $M^*=1238$-MeV resonance *only*, were taken at 31° and 90°. These are presented as *averages* over the resonance, and are averaged over an interval $\Delta K=150$ MeV, centered on $K=325$ MeV.

Excitation of the $M^*=1238$-MeV Resonance

The most obvious feature of the scattered electron spectra, after the elastic scattering itself, is the peak at the mass $M^*=1238$ MeV. This is well known, has been the object of previous studies, and will now be discussed. A treatment based on relativistic dispersion relations of the photoproduction of this resonance was first presented by Chew, Goldberger, Low, and Nambu[7] (CGLN). This was later extended to electroproduction by Fubini, Nambu, and Wataghin[8] (FNW) and further refined by Zagury,[9] and by Adler.[10]

TABLE IV. Differential cross section $d^2\sigma/d\Omega dE_f$ in 10^{-32} cm²/BeV sr, averaged over $\Delta K=150$ MeV centered on $K=325$ MeV.

q^2 (F^{-2}) \ θ	31°	90°
21.4	no measurement	0.855
25.9	4.93	no measurement
35.3	no measurement	0.236
40.1	1.24	no measurement

The CGLN theory assumes that the (3,3) resonance dominates the dispersion integrals and the resonance position is taken from experiment. Then an effective-range relation is obtained for the resonant P phase shift and the small S, D, and nonresonant P phases are derived. The theory was applied firstly to pion-nucleon scattering and then to photoproduction. FNW, using a static model, extended the theory to electroproduction.

In its simple form, the theory had only a qualitative success. A modified form was first used by Hand.[2] Hand recognized that the relation between pion-nucleon scattering and photoproduction is more definite than other features of the theory and took pion-nucleon phases from the experiment. He thereby achieved the first good success of the theory in fitting the total cross sections with no free parameters.

More recently, Höhler[11] has retained the Born terms and the resonant amplitude and neglected the contribu-

[7] G. F. Chew, M. L. Goldberger, F. E. Low, and Y. Nambu, Phys. Rev. **106**, 1345 (1957).
[8] S. Fubini, Y. Nambu, and V. Wataghin, Phys. Rev. **111**, 329 (1958).
[9] N. Zagury, Phys. Rev. **145**, 1112 (1966).
[10] S. Adler, in Proceedings of the Argonne International Conference on Weak Interactions, 1965, Argonne National Laboratory Report No. ANL-7130 (unpublished).
[11] G. Höhler and W. Schmidt, Ann. Phys. (N. Y.) **28**, 34 (1964).

tion of the small phases, which calculation was in any case open to question. He obtained good fits to differential cross section and polarization data, except near $\theta=0°$, where the small terms are important. Adler follows the treatment of Höhler and extends it to electroproduction. The results are equivalent to those of Hand, but he uses a better approximation for electroproduction than the static model of FNW, and his results differ at high-momentum transfers.

The relation between photoproduction and pion-nucleon scattering inherent in CGLN and exploited by Hand, Höhler, and now by Zagury and Adler, was foreshadowed in a theorem due to Fermi and Watson: The phase of the photoproduction amplitude must be the same as that of the pion-nucleon scattering amplitude until inelastic channels in the scattering open up. This holds only for the first ($M=1238$ MeV) resonance; the higher resonances show great inelasticity and an equivalent relation has not been found.

The isobar model of Gourdin and Salin,[12] extended to electroproduction by Loubaton,[13] is superficially different. The results are, however, equivalent. The model automatically satisfies the Fermi-Watson theorem, and the parameters are fitted to pion-nucleon scattering. Likewise, inelasticity limits its usefulness to the first resonance.

An examination of the equations of FNW shows that the dominant part of the electroproduction amplitude is indeed the resonant (3,3) term. The principal variation is according to the formula

$$\sigma_T \propto [G_{MV}(q^2)]^2 |\mathbf{q}|^2, \tag{19}$$

with a slight falloff at higher-momentum transfers. (It is in the details of this falloff that Adler and Zagury improve on FNW.)

Now $G_{MV}(q^2)$ is not completely determined. Although $G_{Mp}(q^2)$ is measured by the elastic cross sections concomitant to this experiment, $G_{Mn}(q^2)$ is quite poorly known at high-momentum transfers. The best guess available is that the form factors are well approximated by a "4-pole fit."[14] Some more recent elastic electron-proton data[15] suggest that G_{Mp} may be lower than suggested by this 4-pole fit.

Figures 10, 11, and 12 show the absolute differential cross sections for the resonance $M^*=1238$ MeV compared to Adler's theory. (Adler and Zagury agree, so it is only necessary to compare to one of them). The data lie 30 to 100% above the calculated curve—a fact already noted by Hand[2] at lower-momentum transfers. The theory of Adler uses a value of G_{MV} given by the 4-pole fit (Table VII). The 4-pole fit gives a value for

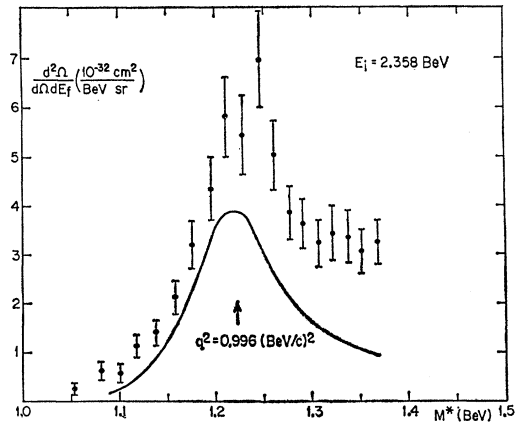

FIG. 10. Excitation of the resonance $M^*=1238$ MeV compared to Adler's theory, for the data of Fig. 7 and Table I.

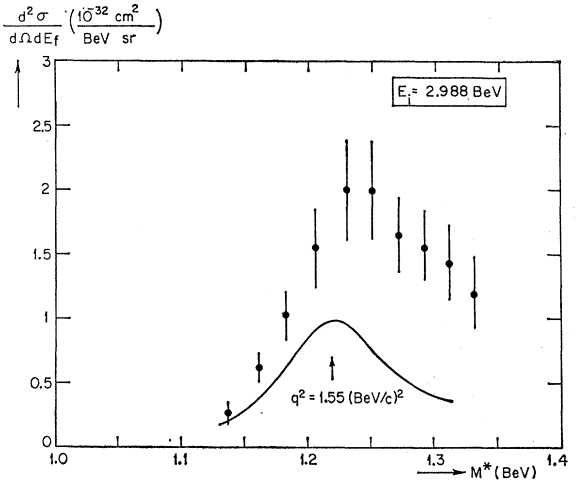

FIG. 11. Excitation of the resonance $M^*=1238$ MeV compared to Adler's theory for the data of Fig. 8 and Table II.

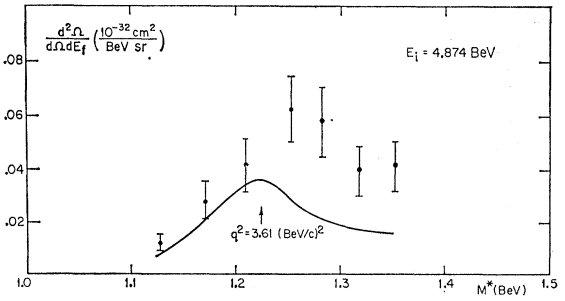

FIG. 12. Excitation of the resonance $M^*=1238$ MeV compared to Adler's theory for the data of Fig. 9 and Table III. Adler's calculations are normalized to a 4-pole fit to elastic scattering (Ref. 4) which lies about 1.4 times the present elastic-scattering results. His calculations are therefore high.

$(G_{Mp})^2$ higher than the data of Ref. 4 by 20% and higher than the data to which this work is now normalized by 50%. Thus the discrepancy is larger than appears directly in Fig. 12. We consider agreement with this

[12] M. Gourdin and Ph. Salin, Nuovo Cimento **27**, 193, 309 (1963).
[13] J. P. Loubaton, Nuovo Cimento **39**, 591 (1965).
[14] L. H. Chan, K. W. Chen, J. R. Dunning, N. F. Ramsey, J. K. Walker, and Richard Wilson, Phys. Rev. **141**, 1298 (1966).
[15] W. Bartel, B. Dudelzak, H. Krehbiel, J. M. McElroy, U. Meyer-Berkhout, R. J. Morrison, H. Nguyen-Ngoc, W. Schmidt, and G. Weber, Phys. Rev. Letters **17**, 608 (1966).

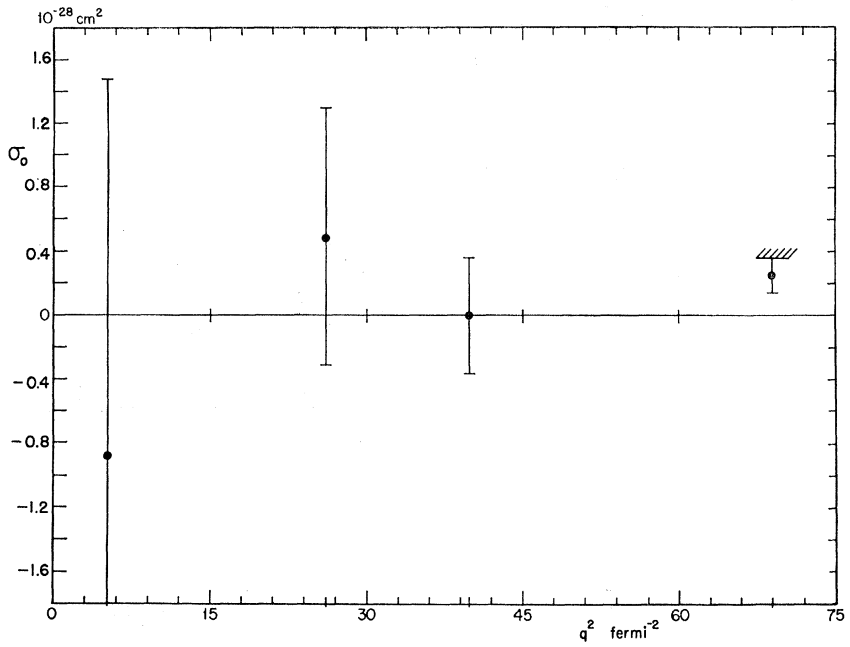

FIG. 13. σ_0 for $M^*=1238$ MeV as a function of momentum transfer.

accuracy at these high-momentum transfers as a remarkable triumph of theory.

There seems to be a shift in the position of the peak towards higher values of M^* from the 1220 MeV predicted by the theory (the theoretical peak is *not* at the mass 1238 MeV). This shift is about $2\frac{1}{2}\%$ in M^* and we believe it is largely real. The magnet calibration was checked (to better than 0.5%) with elastic scattering ($M=938$ MeV) and we believe the magnet's effective length and field gradient to be reproducible to 0.4% and 0.3%, respectively, as functions of the magnet current.

We could interpret the comparison of theory and experiment as a measure of $[G_{MN}(q^2)]^2$. From what we have just said $[G_{MV}(q^2)]^2$ must be raised by 30% and $G_{MV}(q^2)$ by 15% to fit the data. Since $G_{Mp}(q^2)$ is fixed, G_{Mn} must be increased 30% from the 4-pole fit.

FNW predicts that there is no electric quadrupole excitation of the resonance, but there is evidence for a 3–5% admixture of the electric quadrupole and the mag-

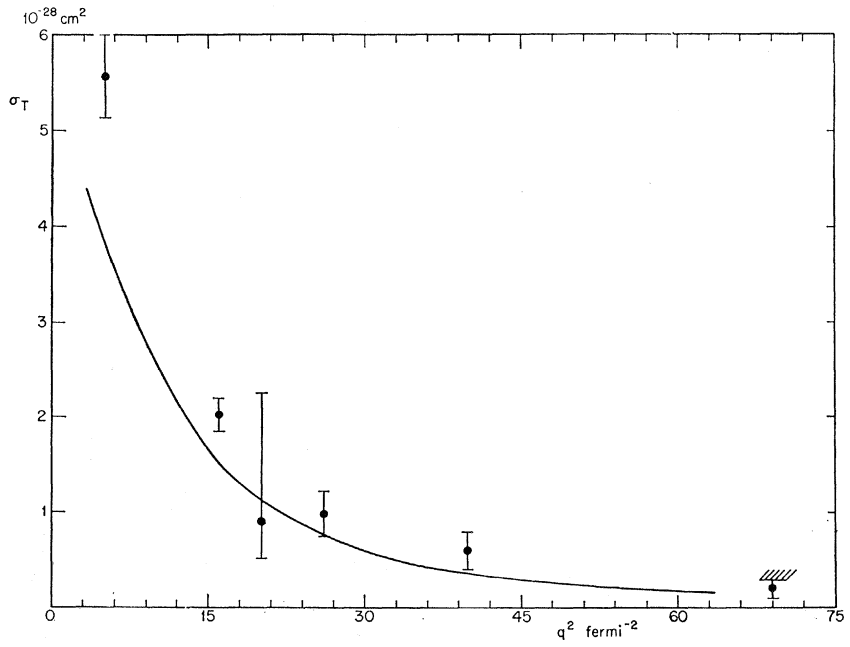

FIG. 14. σ_T for $M^*=1238$ MeV as a function of momentum transfer.

netic dipole excitation. This evidence comes from the angular distribution of recoil protons in π^0 photoproduction at resonance using polarized photons[16] and the equivalent experiment with electron scattering, the angular distribution of the protons in coincidence with electrons scattered inelastically from protons exciting the resonance.[17]

Associated with the electric quadrupole excitation there will be, in general, some longitudinal (scalar) excitation. This can be separated by an angular-distribution method, just as G_E and G_M may be separated in elastic scattering.

Hand[2] already showed that $\sigma_0/\sigma_T<0.3$ at $q^2=5$ F^{-2}. By use of our measurements at $\theta=90°$ (Table IV), we can put upper limits on σ_0 as shown in Table V. We plot σ_0 and σ_T against q^2 in Figs. 13 and 14, together with the theory ($\sigma_0=0$ and solid line for σ_T). Our data are nowhere near precise enough to find the expected value of σ_0 from the known electric quadrupole excitation.

General Theory of Resonance Excitation

Although the theory of excitation of the resonance at $M^*=1238$ MeV is good, no such theory exists for higher resonances. In pion-nucleon scattering, inelastic channels are open[18] and there is considerable inelasticity in the scattering amplitude. The Fermi-Watson theorem does not then apply and a dispersion theory such as that of CGLN cannot be easily justified.

Some general statements can, however, be made about the excitation of resonances. These are well known in the realm of nuclear physics and are extensively used. We here refer to a review paper by Barber.[19] In the nuclear-physics problem, the approximation is usually made of no nuclear recoil (for elementary particles this is the static model). A multipole expansion may then be carried out in the laboratory reference frame. The results derived are valid in the long-wavelength limit $qr\ll1$, where r is the interaction radius, which is presumed to be of the order of the nuclear radius r_0. In elementary-particle physics, the results derived in the long-wavelength limit are sometimes called threshold conditions and we are usually far from $qr\ll1$.

The calculations of σ_T involves the squared matrix element

$$\sigma_T\propto\left|\int\frac{j_l(qr)Y_{l0}(\theta'\phi')\rho(r)}{|\mathbf{q}|}d^3r\right|^2, \tag{20}$$

where $\rho(r)$ is an interaction density which is nonzero only for $r<r_0$, and $\mathbf{q}$ is the 3-dimensional momentum transfer.

[16] D. J. Drickey and R. F. Mozley, Phys. Rev. **136**, B543 (1964).
[17] C. W. Akerlof, W. W. Ash, K. Berkelman, and M. Tigner, Phys. Rev. Letters **14**, 1036 (1965).
[18] A. Donnachie, A. T. Lea, and C. Lovelace, Phys. Letters **19**, 146 (1965).
[19] W. C. Barber, Ann. Rev. Nucl. Sci. **12**, 1 (1962).

TABLE V. Experimental σ_T and σ_0 for $N^*(1238)$ (in 10^{-32} cm^2/BeV sr).

q^2 (F^{-2})	σ_T	σ_0
25.9	0.98±0.25	0.5±0.8
40.1	0.59±0.2	0.0±0.36

The full calculation[19] yields for magnetic transitions of order l (sometimes called abnormal parity transitions):

$$\sigma_T(q^2,K)=(\mathbf{q}/K)^{2l}\sigma_\gamma(K),\qquad \sigma_0(q^2,K)=0; \tag{21}$$

and for electric transitions of order l (often called normal parity transitions) except monopole:

$$\sigma_T(q^2,K)=(\mathbf{q}/K)^{2l-2}\sigma_\gamma(K),$$
$$\sigma_0(q^2,K)=2\frac{l}{l+1}\left|\frac{\mathbf{q}}{K}\right|^{2l-2}\frac{q^2}{K^2}\sigma_\gamma(K)$$
$$=2\frac{l}{l+1}\frac{q^2}{K^2}\sigma_T(q^2,K). \tag{22}$$

Bjorken and Walecka[20] derive similar formulas for σ_T including nuclear recoil. However, they find (again for the case where electric multipoles dominate)

$$\sigma_0(q^2,K)=2(l/(l+1))(q^2/q_0^{*2})\sigma_T(q^2,K). \tag{23}$$

In the static model and long-wavelength limit, this is the same as Eq. (22) because $q_0^*=K$ for $M^*\approx M$ and $q^2=0$.

We note the kinematical relationship

$$|\mathbf{q}^*|M^*=|\mathbf{q}|M. \tag{24}$$

This makes it immaterial which initial or final nucleon system reference frame we use for Eqs. (21) and (22), provided that K is measured in the same frame. At $q^2=0$,

$$|\mathbf{q}^*|/K^*=|\mathbf{q}|/K=1. \tag{25}$$

Equation (23) depends on the following theorems (Ref. 20):

$$\lim_{|\mathbf{q}^*|\to0}(L_{l-}/E_{l-})=-(l-1)/l \quad \text{for} \quad l\geq2,$$
$$\lim_{|\mathbf{q}^*|\to0}(L_{l+}/E_{l+})=1 \quad \text{for} \quad l\geq0,$$

and

$$M_{l\pm}\to|\mathbf{q}^*|^l \quad \text{for} \quad l\geq1, \tag{26}$$

where $M_{l\pm}$, $E_{l\pm}$, and $L_{l\pm}$ are the magnetic, electric, and longitudinal (scalar) multipole coefficients, respectively.

When $q_0^*=0$, it can be shown that all the $L_{l\pm}$ vanish[21]; thus the L/E behavior for small $|\mathbf{q}^*|$ breaks

[20] J. D. Bjorken and J. D. Walecka, Ann. Phys. (N. Y.) **38**, 35 (1966).
[21] S. Adler (private communication).

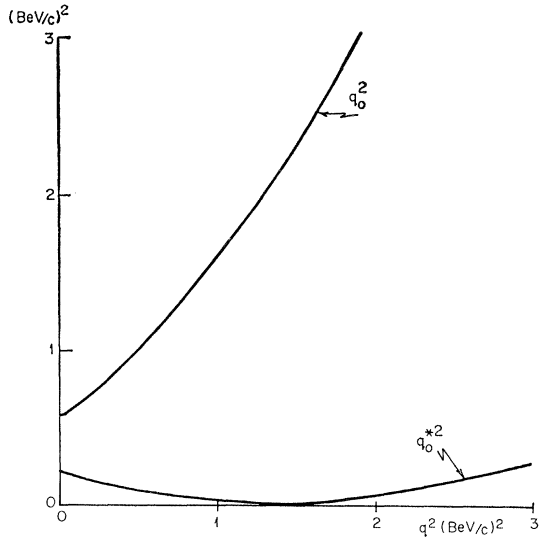

FIG. 15. q_0^2 and q_0^{*2} as a function of q^2 at a mass $M^*=1512$ MeV, illustrating the difficulty of choosing q_0^* in the formula of Eq. (22) or Eq. (23).

down and it is not known what the theoretical ratio of σ_0/σ_T is.

For curiosity's sake, the ratios of $\sigma_0/2\sigma_T$ according to various prescriptions are given for three points of interest in Table VI. Likewise, the behavior of q_0^2 and q_0^{*2} as functions of q^2 is shown in Fig. 15.

The formulas given above for the long-wavelength limit (threshold condition) certainly do not apply to our case where $|q|r\sim 1$ (and do not even apply well for nuclear physics). One must multiply Eqs. (21) and (22) by some arbitrary form factor. At first sight, it is not clear that we have achieved anything by all this maneuvering; we started with an arbitrary function $\sigma_T(q^2,K)$ and still have an arbitrary function $F^2(q^2,K)$. But the form factor is now expected to be characteristic of the nucleon size. If we refer back to Eq. (20), we may guess the interaction density to be equal to the nucleon size. This may be approximated (Ref. 3) by an exponential $e^{-\lambda r}$ which is the Fourier transform of the form factor:

$$F(q^2)\propto[1+q^2/(0.72)]^{-2}, \tag{27}$$

according to

$$\left|\int j_0(qr)e^{-\lambda r}d^3r\right|^2\propto|F(q^2)|^2. \tag{28}$$

For the magnetic dipole transition to $M^*=1238$ MeV,

TABLE VI. Theoretical $\sigma_0/2\sigma_T$ for the resonance $N^*(1512)$.

Prescription \ q^2 (BeV/c)²	0.797	1.31	3.30
$[l/(l+1)]q^2/K^2$	0.797	1.18	2.96
$[l/(l+1)]q^2/q_0^2$	0.295	0.312	0.262
$[l/(l+1)]q^2/q_0^{*2}$	9.96	601.0	4.12

for example, we find that

$$\left|\int j_1(qr)e^{-\lambda r}d^3r\right|^2\propto q^2|F(q^2)|^2. \tag{29}$$

The relevant form factor is clearly the magnetic vector form factor $G_{MV}(q^2)$, and we find therefore the recipe of Eq. (19) which we found earlier was the dominant term in the FNW dispersion-theory calculation, but not including the kinematic factors included by Adler.

For the other resonances, the theory is less certain for many reasons. At the start of this work, resonances were known at $M^*=1512$ MeV ($I=\frac{1}{2}$, $J=\frac{3}{2}^-$) and $M^*=1688$ MeV ($I=\frac{1}{2}$, $J=\frac{5}{2}^+$) from pion-nucleon scattering and photoproduction. Since then, phase-shift analyses of pion-nucleon scattering[18] have shown the existence of other resonances superimposed at these energies. The disentanglement of their contributions to photoproduction has not been performed, and it would be harder for electroproduction (for which there are less data). We shall proceed to analyze the data on the supposition of only these two (old) resonances—plus a background—and endeavor to derive what information we can. As we shall see, no amount of contribution of the new resonances can affect a peculiarity of the excitation at $M^*=1512$ MeV.

Another uncertainty is what form factor to use for these resonances. For a resonance dominated by transverse excitation, the magnetic form factor is probably appropriate since the "magnetic form factor" is the name given to the transverse elastic form factor. But a transition to a state of $I=\frac{1}{2}$ could involve $G_{MS}(q^2)$ more strongly than $G_{MV}(q^2)$. Now,

$$\begin{aligned}2G_{MS}(q^2)&=G_{Mp}(q^2)+G_{Mn}(q^2)\\&=G_{Mp}(q^2)-|G_{Mn}(q^2)|.\end{aligned} \tag{30}$$

G_{MS} therefore involves a subtraction of two numbers of the same order of magnitude and is very poorly known. For the longitudinal excitation to $I=\frac{1}{2}$ state, probably $G_{ES}(q^2)$ becomes important and the electric form factors are hardly known at all at the momentum transfers of interest here. For the sake of denifiteness, and for no

TABLE VII. Comparison of form factors.

q^2 (BeV/c)²	$G_{MV}^2(q^2)/G_{MV}^2(0)$		$G_{EV}(q^2)/G_{EV}(0)$	
0.996	0.0300	0.0319	0.0462	0.0716
1.55	0.00861	0.0114	0.0265	0.0312
3.61	0.000730	0.0012	−0.0059	0.00637
0.791	0.0494	0.0515	0.0689	0.1010
1.31	0.0152	0.0171	0.0254	0.0445
3.30	0.000972	0.00160	−0.0051	0.00760
0.649	0.0750	0.0751	0.0921	0.1370
1.138	0.0217	0.0237	0.00352	0.0570
3.06	0.00126	0.0019	−0.0042	0.00897
0.424	0.154	0.151	0.1516	0.2344
0.822	0.0461	0.0477	0.0648	0.0981
2.69	0.00190	0.0027	−0.0022	0.01156
	1-parameter [Eq. (27)]	4-pole (Ref. 14)	4-pole	1-parameter

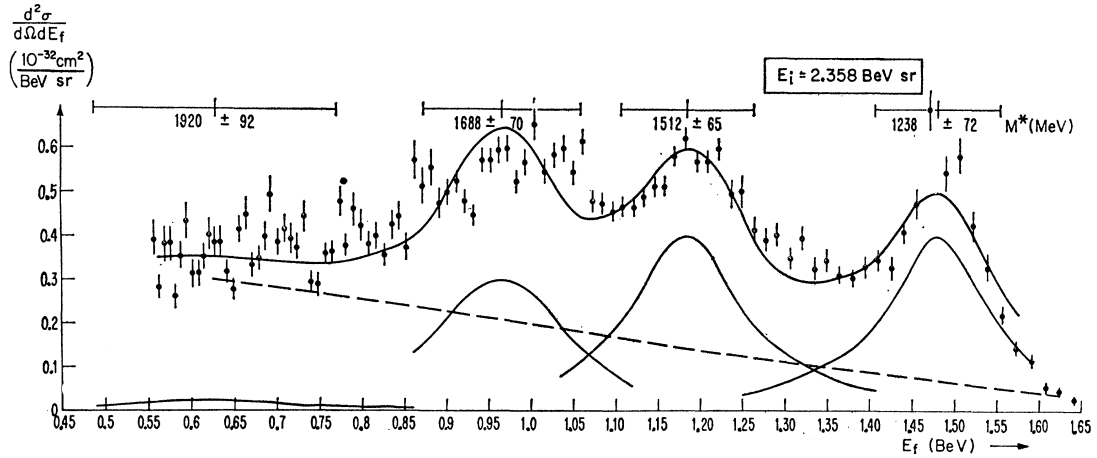

FIG. 16. Spectrum of nucleon excitation from Fig. 7, showing decomposition into resonances.

other reason, we have chosen to compare our results to $G_{MV}(q^2)$ as for the $M^*=1238$-MeV case. Table VII shows how the form factors G_{MV} and G_{EV} might change for two fits which are not far from known data {but note that at $q^2\sim 4$ (BeV/c)^2 the 1-parameter fit [Eq. (27)] does not fit the data to which this experiment is normalized}.

Breit-Wigner Fits and Multipole Fits

The problem arises of the size of the resonant contribution relative to the nonresonant contribution. We understand the first resonance well enough to know that $\frac{1}{4}$ of the photoproduction cross section at the peak is nonresonant. We can see this most easily from the statement that the transition $\gamma+p\rightarrow p+\pi^0$ is entirely resonant, and from Clebsch-Gordan coefficients is twice the resonant cross section in $\gamma+p\rightarrow n+\pi^+$. Yet these two cross sections are experimentally equal, and hence there is a nonresonant background in $\gamma+p\rightarrow n+\pi^+$ equal to $\frac{1}{4}$ of the total γ-absorption cross section.

The nonresonant part falls somewhat faster with increasing momentum transfer than the resonant part and is probably small at $q^2=90$ F^{-2}. In the detailed comparison with theory made earlier for the first resonance, the nonresonant background is, of course, included.

The crude separation of the resonances discussed below is based on the assumption that the widths remain the same as the value at $q^2=0$, and is therefore somewhat arbitrary. In view of these reservations, and those discussed earlier, we still endeavor to make some physical interpretation of the data.

After the radiative corrections were carried out by the Perez y Jorba method, the resonant part of the scattering was estimated from the shapes of the resonances. In trying to determine whether or not a resonance exists, only the statistical errors in Figs. 16, 17, and 18 are significant because the radiative, solid target, and shower-efficiency corrections give smooth curves. The full width at half-height was calculated *a*

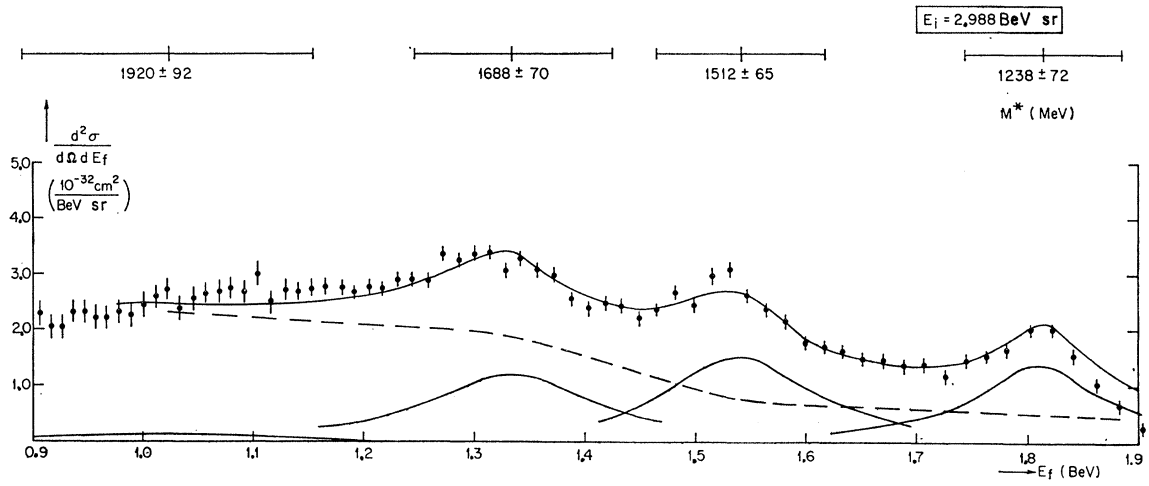

FIG. 17. Spectrum of nucleon excitation from Fig. 8, showing decomposition into resonances.

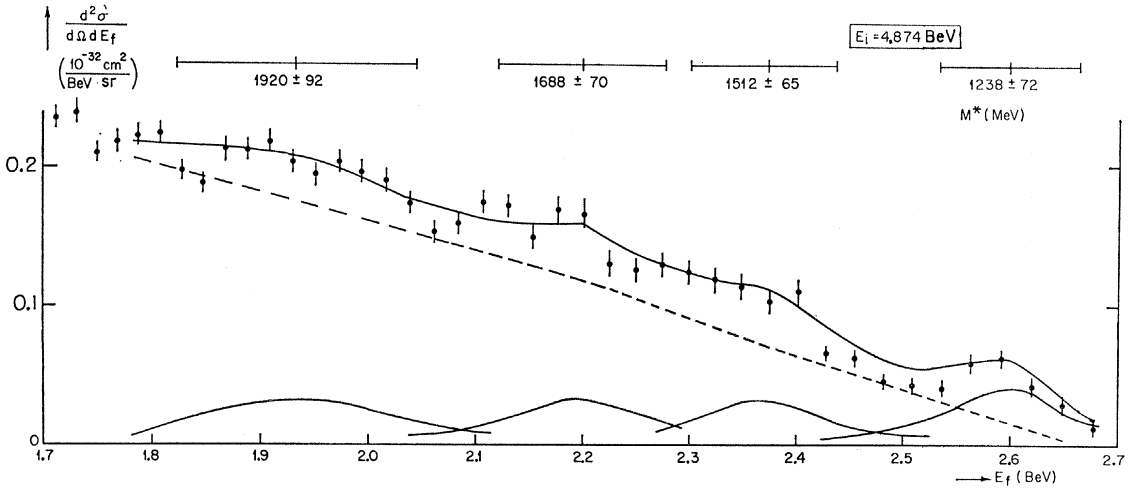

FIG. 18. Spectrum of nucleon excitation from Fig. 9, showing decomposition into resonances.

priori, for each of the four resonances, [$N^*(1238)$, $N^*(1512)$, $N^*(1688)$, and $N^*(1920)$] and at each of the three incident energies (2.358, 2.988, and 4.874 BeV), assuming widths of 130, 140, 145, and 185 MeV, respectively.

The scattered energies and widths at which these resonances were expected to be observed were calculated from kinematics. To these were added in quadrature the width of the elastic peak (i.e., at corresponding incident energies) to obtain the expected experimental width of each resonance at each incident energy.

Half of the resonant contribution was then assumed to be the difference between the cross section at the peak of the resonance and the average of the cross section, a half-width either side of the peak. These amplitudes are shown in Table VIII. The crudeness of this method introduces large uncertainties which have been estimated to be anywhere from a factor of $1\frac{1}{4}$ to a factor of 4, depending on how clearly the resonance stands out.

If we assume a resonant structure of the form

$$\left.\frac{d^2\sigma}{dE_f d\Omega}\right|_{\text{resonant}}=\frac{A\Gamma^2/4}{(E_f-E_{\text{res}})^2+\Gamma^2/4}, \tag{31}$$

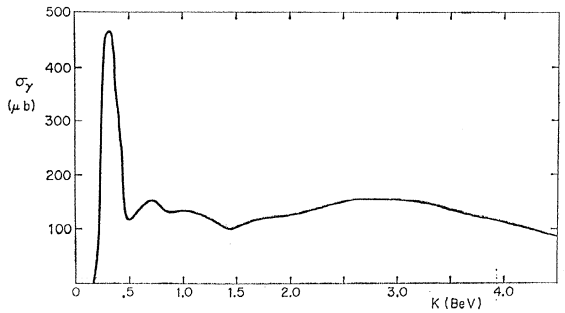

FIG. 19. Total photoproduction cross section taken from existing data.

we find the average from $E_{\text{res}}-\frac{1}{2}\Gamma$ to $E_{\text{res}}+\frac{1}{2}\Gamma$ to be

$$d\sigma/d\Omega|_{\text{resonant}}/\Gamma_{Ef}=\tfrac{1}{4}\pi A. \tag{32}$$

This permits us to use the peak amplitude in estimating the multipole fits.

The nonresonant contribution to the scattering was then assumed to be what was left after the contributions of the four resonances were removed. Figures 16, 17, and 18 show the inelastic spectrum after radiative corrections (the points with the bars), the contribution of each resonance (smooth bell-shaped curves), the assumed nonresonant scattering (dashed line), and the reconstructed spectrum, i.e., the sum of the assumed nonresonant and of all four resonances (single smooth line).

Figure 19 shows the total cross section for photoproduction as compiled from the data for

$$\begin{aligned}
p+\gamma &\rightarrow p+\pi^0\\
&\rightarrow n+\pi^+\\
&\rightarrow p+\pi^++\pi^-\\
&\rightarrow p+\pi^++\pi^-+\pi^0+(\gamma\pi^0)\\
&\rightarrow n+\pi^++\pi^++\pi^-+(\gamma\pi^0)\\
&\rightarrow p+2\pi^++2\pi^-+(\gamma\pi^0)\\
&\rightarrow n+3\pi^++2\pi^-\\
&\rightarrow \text{strange particles}.
\end{aligned}$$

For some purposes, it is more convenient to use the cross section integrated over the resonance, i.e., $d\sigma/d\Omega|_{\text{over resonance}}$. Accordingly the values of

$$\int_{-\infty}^{\infty}\frac{A\Gamma^2/4}{(E_f-E_{\text{res}})^2+\Gamma^2/4}dE_f=\tfrac{1}{2}\pi A \tag{33}$$

are given in Table IX.

The values of σ_T used in the multipole fits were

TABLE VIII. Areas under the resonances, $\frac{1}{2}\pi A\Gamma$ (10^{-32} cm^2/sr).

Resonance (BeV) \ Incident energy (BeV)	2.358	2.988	4.874
1.238	0.92	0.312	0.0082
1.512	0.98	0.36	0.0069
1.688	0.89	0.33	0.0078
1.920	0.09	0.04	0.0112 (upper limits)

obtained from the data in Table VIII and the following formulas:

For $N^*(1238)$ and $N^*(1920)$, according to Eq. (1) and the rule stated after Eq. (23),

$$d^2\sigma/d\Omega dE_f=\sigma_T(q^2,K)\Gamma_T(\theta,q^2,K); \quad (34)$$

and for $N^*(1512)$ and $N^*(1688)$, according to Eqs. (1) and (23),

$$\frac{d^2\sigma}{d\Omega dE_f}=\sigma_T(q^2,K)\left[\Gamma_T(\theta,q^2,K)+\frac{2l}{l+1}\frac{q^2}{K^2}\Gamma_0(\theta,q^2,K)\right], \quad (35)$$

and $l=1$ or 2 for $N^*(1512)$ or $N^*(1688)$, respectively. The values for $\sigma_T(q^2,K)$ thus obtained are given in Table IX.

As a test of Eqs. (21) and (22) the values of the logarithm of σ_T/G_{MV}^2 are plotted against the logarithm of $|\mathbf{q}^2|$ for constant M^*. The results are shown in Figs. 20, 21, and 22.

By reason of the previously indicated arguments about change in angular momenta, isotopic spin, and parity, we expect the excitation of the resonances to go as indicated by the dashed lines.

Comparison of these assignments (summarized in Table X) with Figs. 20, 21, and 22 shows rather remarkable agreement considering the approximations that entered into the calculations. A possible deviation exists at 1512, where the electric dipole excitation prediction does not simultaneously fit the photoproduction and electroproduction data. The new resonances would

TABLE IX. "Theoretical" $\sigma_T(q^2,K)$ in 10^{-28} cm^2 as extracted from Eqs. (35) and (36).

Resonance Momentum transfer	q^2 (BeV/c)^2	0.996	1.55	3.61
K=0.346 BeV	σ_T	1.06	0.62	0.0520
M^*=1238 MeV				
Resonance Momentum transfer	q^2 (BeV/c)^2	0.797	1.31	3.30
K=0.746 BeV	σ_T	0.34	0.15	0.0046
M^*=1512 MeV				
Resonance Momentum transfer	q^2 (BeV/c)^2	0.649	1.138	3.06
K=1.045 BeV	σ_T	0.32	0.11	0.0061
M^*=1688 MeV				
Resonance Momentum transfer	q^2 (BeV/c)^2	0.424	0.822	2.69
K=1.50	σ_T	0.032	0.021	0.0016
M^*=1920 MeV				

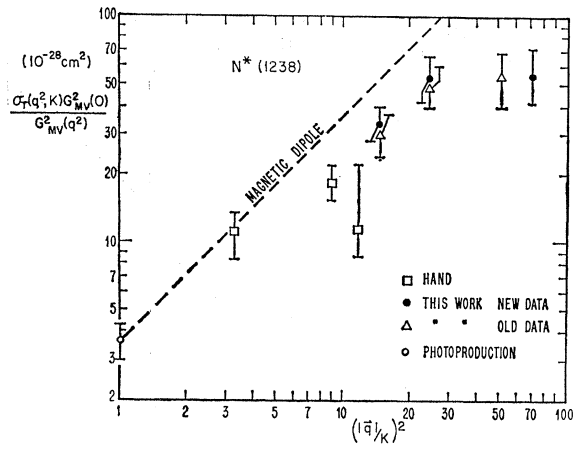

FIG. 20. The resonant $M^*=1238$-MeV cross section plotted against $(|\mathbf{q}|/K)^2$ showing the fall away from the magnetic dipole dependence. Data from two runs are shown.

be excited by electric monopole and dipole excitation. Possible reasons for the discrepancy are the replacement of q_0^* by K [use of Eq. (22) instead of (23)] and use of G_{MV} instead of G_{ES}.

CONCLUSIONS AND SPECULATIONS

The excitation of the resonances at $M^*=1238$ MeV agrees reasonably with theory and further work can identify details. A separation of σ_0 and σ_T by measurements of this type, or by the distribution in the azimuthal angle ϕ of the outgoing protons, can give information

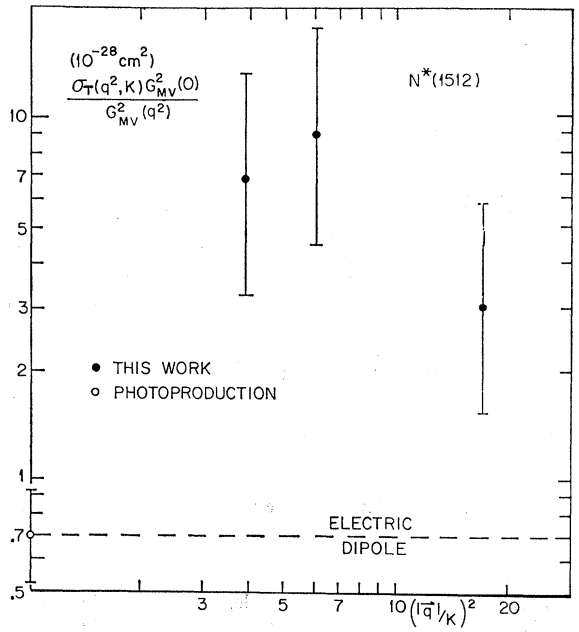

FIG. 21. The resonant $M^*=1512$-MeV cross section plotted against $(|\mathbf{q}|/K)^2$ showing the unusually high-electroproduction cross section.

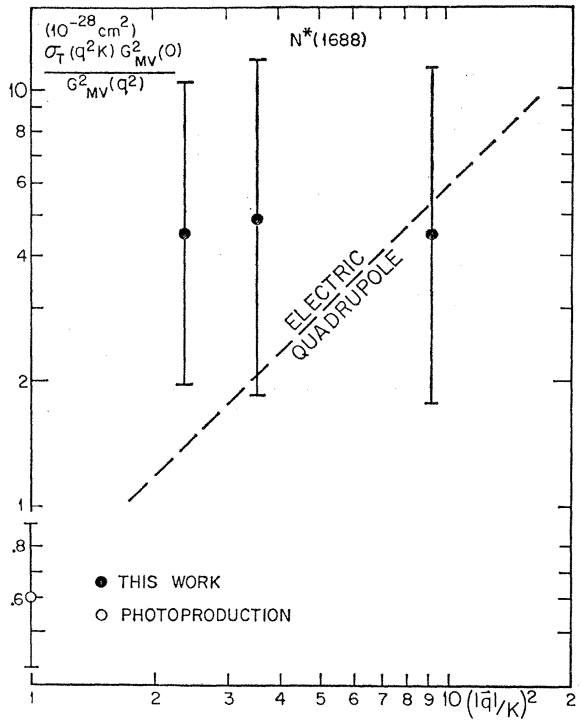

FIG. 22. The resonant $M^*=1688$-MeV cross section showing a fit to electric quadrupole excitation.

on the electric quadrupole admixtures as a function of momentum transfer.

Similar separation at the higher resonances should confirm the assumption that longitudinal transitions play an important role in the production of some of these resonances.

It is interesting to speculate on the excitation of higher resonances. According to present ideas, these should be of high spin corresponding to Regge recurrences (rotational states) of the nucleon and the $M^*=1238$-MeV state. They should then stand out more strongly in electroproduction than photoproduction because of the factor $(\mathbf{q}r)^{2l}$ in σ_T. But this increase has its limits; the relative enhancement in electroproduction should really be considered as a suppression of higher multipoles in photoproduction. When $qr\sim 1$, the threshold behavior clearly breaks down. But a naive use of Eq. (20) suggests a relative enhancement of a factor of 20 for a $J=11/2$ resonance with mass 3 BeV for a momentum transfer of ~ 10 $(\mathrm{BeV}/c)^2$.

TABLE X. First-order multipole dependence of resonances.

		Power of q
$N^*(1238)$,	Magnetic dipole,	$2^1=2$
$N^*(1512)$,	Electric dipole	$2^1-2=0$
$N^*(1688)$,	Electric quadrupole	$2^2-2=2$
$N^*(1920)$,	Magnetic quadrupole,	$2^2=4$

The use of a high-energy accelerator (e.g., SLAC) is clearly indicated for this study both for reaching the high-momentum transfer and for reducing the radiative corrections.

ACKNOWLEDGMENTS

Our thanks go to J. Chen, who assisted in the detailed preparation of this paper, and to the CEA staff for producing accelerated beams without which this work could not have been done. In particular, we would like to acknowledge the assistance of Art Hansen and his crew and also the enthusiastic assistance of the operations group under Dr. G. Voss. The cyclotron laboratory staff, under the direction of M. Wanagel, J. McElaney, D. Wharton, and W. Dunn, ably constructed the apparatus. Much valuable assistance was provided by M. Goitein, R. Budnitz, K. Hanson, A. Liberman, and C. Mistretta.

APPENDIX

Radiative Corrections

Bjorken writes down a formula relating $\sigma_{\mathrm{meas}}(E_i,E_f)$ and $\sigma(E_i,E_f)$:

$$\sigma_{\mathrm{meas}}(E_i,E_f)=\int_0^{E_i} dE_i' \int_{E_f}^{\infty} dE_f' P(E_i,E_i',\delta_i) \times\sigma(E_i',E_f')P(E_f',E_f,\delta_f), \quad \text{(A1)}$$

where $P(E,E',\delta)$ is the probability of an electron of energy E radiating to produce an electron of energy E' with radiator δ.

To include internal radiative effects in the peaking approximation

$$\delta_{i,f}=\frac{\alpha}{\pi}[\ln(q^2/m^2)-1]+t_{i,f}|\ln 2, \quad \text{(A2)}$$

where $t_{i,f}$ are the thickness of the physical radiators in the path of the incident (final) beam in radiation lengths.

Bjorken approximated

$$P(E,E',\delta)=\frac{[\ln(E/E')]^{\delta-1}}{E\Gamma(\delta)}=\frac{\delta}{E\ln E/E'} \quad \text{(A3)}$$

for small δ. Now replace

$$\int_0^{E_i} \text{ by } \int_0^{E_i-\Delta}+\int_{E_i-\Delta}^{E_i}, \text{ and } \int_{E_f}^{\infty} \text{ by } \int_{E_f}^{E_f+\Delta}+\int_{E_f+\Delta}^{\infty},$$

where Δ is the bin size as in the Perez y Jorba recipe.

Then,

$$\sigma_{\text{meas}}(E_i,E_f)=\int_{E_i-\Delta}^{E_i}dE_i'\int_{E_f}^{E_f+\Delta}dE_f'P\sigma P+\int_0^{E_i-\Delta}dE_i'\int_{E_f}^{E_f+\Delta}dE_f'P\sigma P+\int_{E_i-\Delta}^{E_i}dE_i'\times\int_{E_f+\Delta}^{\infty}dE_f'P\sigma P+\int_0^{E_i-\Delta}\int_{E_f+\Delta}^{\infty}P\sigma P. \quad \text{(A4)}$$

Integrate over the interval Δ, and assume

$$\Delta/E_{i,f}\ll 1, \quad \delta\ll 1.$$

Note that

$$\int_{E_i}^{E_f+\Delta}dE_f'\frac{1}{E_f'}\frac{[\ln(E_f'/E_f)]^{\delta_f-1}}{\Gamma(\delta_f)}=\left(\frac{\Delta}{E_f}\right)^{\delta_f}=e^{\delta\ln(\Delta/E_f)}=1+\delta_f\ln(\Delta/E_f)+O(\delta^2), \quad \text{(A5)}$$

and, similarly,

$$\int_{E_i-\Delta}^{E_i}dE_i'\frac{1}{E_i}\frac{[\ln(E_i/E_i')]^{\delta_i-1}}{\Gamma(\delta_i)}\simeq 1+\delta_i\ln\frac{\Delta}{E_i}+O(\delta^2). \quad \text{(A6)}$$

Also note that

$$\int_{E_f+\Delta}^{E_{f\,\max}}\frac{dE_f'}{E_f'}\frac{[\ln(E_f'/E_f)]^{\delta_f-1}}{\Gamma(\delta_f)}=(\ln E_{f\,\max}/E_f)^{\delta}-(\ln(E_f+\Delta)/E_f)^{\delta}=e^{[\delta\ln(E_{f\,\max}/E_f)]}-e^{[\delta\ln\Delta/E_f]}=1-\delta\ln\left(\ln\frac{E_{f\,\max}}{E_f}\right)+O(\delta^2)-\left[1+\delta\ln\frac{\Delta}{E_f}+O(\delta)^{-2}\right]=\delta[\ln(\ln E_{f\,\text{mex}}/E_f)-\ln\Delta/E_f+O(\delta^2)]. \quad \text{(A7)}$$

TABLE XI. Values of radiation kernels (in BeV^{-1}) given by Hand, Bjorken, and the first approximation

$$K=\frac{(\alpha/\pi)[\ln(q^2/m^2)-1]}{E-E'}$$

for $q^2=1$ (BeV/c)^2, $E=1$ BeV.

E'/E	Hand	Bjorken	1st approx.
0.99	3.26	2.9	3.30
0.9	0.298	0.302	0.330
0.8	0.135	0.144	0.165
0.7	0.080	0.089	0.110
0.6	0.057	0.064	0.082
0.5	0.042	0.048	0.066

Hence if we drop all terms in δ^2 and higher, we have

$$\sigma_{\text{meas}}(E_i,E_f)\simeq(1+2\delta\ln\Delta/E_f)\sigma(E_i,E_f)+\int_0^{E_i-\Delta}dE_i'P(E_i,E_i',\delta_i)\sigma(E_i',E_f)+\int_{E_f+\Delta}^{\infty}dE_f'\sigma(E_i,E_f')P(E_f',E_f,\delta_f). \quad \text{(A8)}$$

This shows that to first order in α the Perez y Jorba recipe is equivalent to the Bjorken recipe.

We note here that an additional calculation using the Perez y Jorba recipe with a bin size $\Delta E=0.01$ BeV gave the same results as the calculation with $\Delta E=0.02$ BeV.

We also note that a calculation using the Perez y Jorba recipe with Bjorken's radiation kernels instead of Hand's gave corrected cross sections which differ by less than 1% from the quoted results. A comparison of the radiation kernels for the two cases (Table XI) shows that the differences are unimportant. At first sight, the difference of the Bjorken recipe in the first line seems inconsistent with Eq. (A8) and the statement derived therefrom. In Eq. (A8) the approximation is made that $\delta\ll 1$ which is invalid when E' is close to E.